



Recycled brick aggregates in one-part alkali-activated materials: Impact on 3D printing performance and material properties

Yazeed A. Al-Noaimat^a, Mehdi Chougan^a, Abdulrahman Albar^b, Szymon Skibicki^c, Karol Federowicz^c, Marcin Hoffman^d, Daniel Sibera^c, Krzysztof Cendrowski^c, Mateusz Techman^c, João Nuno Pacheco^e, Sang-Yeop Chung^f, Pawel Sikora^c, Mazen Al-Kheetan^g, Seyed Hamidreza Ghaffar^{a,h,i,*}

^a Department of Civil and Environmental Engineering, Brunel University London, Uxbridge, UB8 3PH, UK

^b Bina Robotics Ltd. CRL, Shipping Building, 252 Blyth Rd., Hayes, UB3 1HA, UK

^c Faculty of Civil and Environmental Engineering, West Pomeranian University of Technology in Szczecin, Al. Piastow 50, 70-311, Szczecin, Poland

^d Faculty of Mechanical Engineering and Mechatronics, West Pomeranian University of Technology in Szczecin, Al. Piastow 19, 70-310, Szczecin, Poland

^e c5Lab – Sustainable Construction Materials Association, Edificio Central Park, Rua Central Park 6, 2795-242, Linda-a-Velha, Portugal

^f Department of Civil and Environmental Engineering, Yonsei University, Seoul, 03722, Republic of Korea

^g Department of Civil and Environmental Engineering, College of Engineering, Mutah University Mutah, Karak, 61710, P.O. BOX 7, Jordan

^h Applied Science Research Center, Applied Science Private University, Jordan

ⁱ School of Engineering, University of Birmingham, Dubai International Academic City, Dubai P.O. Box 341799, United Arab Emirates

ARTICLE INFO

Keywords:

3D printing
One-part alkali-activated materials
Brick powder
Brick aggregate
Buildability

ABSTRACT

This study investigates the printability of one-part brick powder-based alkali-activated materials (AAMs) containing end-of-life brick particles as aggregate. The novel formulation showcases promise for 3D printing of small to medium-sized building blocks, reminiscent of a Lego-type system, capitalising on the rapid setting time inherent to one-part AAMs. The effect of replacing up to 50% by weight of natural aggregate with brick aggregate on the fresh properties of brick powder-based alkali-activated materials, including slump measurements, flowability, setting time, open time and green strength were investigated. In addition, the flexural and compressive strength of the 3D printed mixtures were determined and compared to those of cast specimens. The buildability and microstructure were also examined. The results showed that incorporating high porous and rough brick aggregate to replace natural aggregate is beneficial in improving the mixtures' slump, which is essential for retaining the shape of the printed layers. However, it decreased the flowability, setting time and open time when incorporating up to 50% brick aggregate. The green, flexural and compressive strengths were increased with increasing brick aggregate content up to 50% due to enhancing interlock between the binder and brick aggregate, and the better compaction because of the absorption properties of brick aggregate. The mechanical results revealed the better performance of 3D printed specimens than the cast specimens. Moreover, the incorporation of brick aggregate enhanced the buildability of the mixtures showcasing their potential in advancing 3D printing capabilities.

1. Introduction

The construction sector faces challenges in reducing waste, greenhouse gas emissions, and natural resource consumption. In response to the aforementioned challenges, the construction industry has embraced a novel technique known as concrete 3D printing. This method boasts numerous advantages when compared to traditional construction

methods, including reducing construction costs and time by eliminating the need for expensive formwork and high labour numbers, providing environmental benefits (Agusti-Juan et al., 2017; Weng et al., 2020), reducing waste (Markin et al., 2021; Adaloudis and Bonnin Roca, 2021), and allowing for diverse and complex architectural designs (Menna et al., 2020; Yu et al., 2020). In addition, it decreases the overuse of natural aggregate (NA) compared to the traditional concrete production

* Corresponding author. Department of Civil and Environmental Engineering, Brunel University London, Uxbridge, UB8 3PH, UK.

E-mail addresses: seyed.ghaffar@brunel.ac.uk, s.h.ghaffar@bham.ac.uk (S.H. Ghaffar).

<https://doi.org/10.1016/j.dibe.2023.100248>

Received 8 August 2023; Received in revised form 23 September 2023; Accepted 6 October 2023

Available online 12 October 2023

2666-1659/Crown Copyright © 2023 Published by Elsevier Ltd. This is an open access article under the CC BY license (<http://creativecommons.org/licenses/by/4.0/>).

methods (Yang et al., 2023). 3D printed concrete requires more binder and smaller aggregate content for easier extrudability than traditional concrete (Al-noaimat et al., 2023a). This decreases the viability of this technology by increasing the demand for ordinary Portland cement (OPC), whose production is an energy-intensive process with huge negative environmental impacts (Xu et al., 2021; Zhao et al., 2023; Charkhtab Moghaddam et al., 2021; Al-noaimat et al., 2023b; Al-noaimat and Akis, 2023). In this regard, alkali-activated materials (AAMs) have attracted researchers' interest during the last decade due to their capability to lower the CO₂ footprint produced by conventional concrete (Chen et al., 2022; Chougan et al., 2022). AAMs are produced by alkaline activating precursors containing materials rich in alumina or/and aluminosilicate, such as silica fume (SF), fly ash (FA) and ground-granulated blast furnace slag (GGBS). AAM could be classified into two categories depending on the alkaline activators' physical form: two-part AAM prepared using a liquid activator and one-part AAM prepared using a solid activator. One-part AAM prepared with a solid activator was developed to overcome the handling problem of the hazardous liquid activator and thus enable AAMs' broader practical applications, including 3D printing (Adesanya et al., 2018; Luukkonen et al., 2018a, 2018b). However, due to its rapid strength growth and fast setting time, one-part AAM distinctly suits the fabrication of modestly sized objects, encompassing prototyping as well as the construction and assembly of infrastructure elements like walls and columns. Although AAMs exhibit superior performance over that of conventional concrete (El-seidy et al., 2023; Farhan et al., 2019), some challenges restricts its employability in the different applications, including shrinkage (Zhang et al., 2022a). However, some methods were proposed to mitigate this problem, such as incorporation of chemical additives (Zhang et al., 2022b).

Besides the sorted problem of liquid activators, another obstacle is that the most common precursors used in AAM (i.e., FA, SF, and GGBS) are not available in some countries and their availability will severely decrease in the upcoming years due to significant efforts toward reduction of carbon dioxide. Thus, it is crucial to introduce alternative binder materials (Migunthanna and Rajeev, 2022). Meanwhile, construction and demolition waste (CDW) amounts are gradually increasing with the increase in construction industry activities, population, and urbanisation. Around 45% of CDWs, excluding soils, are brick and ceramic wastes (Oikonomou, 2005; Reig et al., 2013; Fatta et al., 2003). The disposal of brick and ceramic waste in landfills is a costly and ecologically detrimental practice that also consumes precious land resources (Dadsetan et al., 2019; Lu, 2019; Robayo et al., 2016; Ouda and Gharieb, 2020). Various studies have examined brick as an aggregate in mixtures, with mixed results regarding its impact on performance. While incorporating brick aggregate (BA) can diminish durability by increasing the transport properties of mixtures (Paul et al., 2018; Dang et al., 2018), it improves thermal and acoustic insulation (Dang et al., 2018) and decreases drying shrinkage. This is because BA has high water absorption and releases water to the binder matrix as the binder loses water during hydration and moisture exchange with the environment, thereby facilitating internal curing (Zhang et al., 2018; Wong et al., 2018).

Employing end-of-life bricks as a binder in AAMs presents a suitable approach to overcome high demands on OPC production and massive amounts of CDW disposal problems. Several studies have attempted to use end-of-life bricks, due to its high alumina and silica content in their chemical composition, as a pozzolanic material to partially replace OPC and as a binder in AAMs (El-gamal et al., 2017; Puertas et al., 2008), (Hwang et al., 2019; Allahverdi and Kani, 2013; Ilcan et al., 2022). Migunthanna et al. (2021) investigated the effect of incorporating different brick powder (BP) percentages in one-part geopolymer. They found that the mixture containing 40% BP and 60% GGBS achieved a compressive strength of 48 MPa after 7 days of curing. Most recently, Pasupathy et al. (2023) investigated the suitability of using brick powder as a precursor in one-part AAM for 3D concrete printing. Their study

demonstrated that substituting 10% of FA with BP improved the mechanical properties of cast and 3D printed mixtures by up to 12%. However, further increasing the BP content negatively impacted the strength of the materials. Moreover, it was reported that the compressive strength of printed samples was highest when loaded longitudinally along the printing direction. This was slightly lower than cast samples or samples loaded perpendicularly or laterally. Various studies have examined the properties of cast and 3D-printed one-part AAM made from different precursor materials, but research on brick-based AAM is limited. To the best of authors' knowledge, no studies have investigated the printability and the performance of 3D-printed brick-based one-part AAM containing BA. The novel approach of utilising high content of end-of-life CDW in different forms (i.e., aggregate and binder) aligns with circular economy principles aimed at reducing the generated waste and over-exploitation of raw materials. Accordingly, this study investigates the feasibility of using end-of-life brick as aggregates to replace natural aggregates with different percentages and evaluates the effect on the fresh, hardened and printing properties of one-part brick powder-based AAM.

2. Materials and methods

A schematic overview of the experimental programme is presented in Fig. 1.

2.1. Materials

Ground-granulated blast furnace slag (GGBS) obtained from Hanson, UK, and brick processed into powder from demolition sites near Brunel University London, UK, were used as the precursor materials. Sodium metasilicate (Na₂SiO₃) in powder form obtained from Fisher Scientific, UK, with a purity of 97.5% and alkalinity modulus (SiO₂/Na₂O) of 1.6, was used as the alkali activator. The chemical oxides of the materials used in the precursor were determined using XRF and are shown in Table 1. The mineralogical compositions, physical and microstructural characteristics of the different materials, and preparation process of brick powder can be found in the following reference (Al-noaimat et al., 2023c). The NA used was siliceous river sand with a grading of 0–2 mm. The NA was used as delivered by the supplier and are certified for use in concrete according to BS EN 12620:2013 (BS EN 12620, 2013). The brick aggregate (BA) was produced by crushing the waste brick, followed by sieving to impose a grading distribution with particle size between 1 and 2 mm. The testing protocol of the NA followed the tests presented in BS EN 12620:2013 (BS EN 12620, 2013) and included the testing of properties that are relevant for the fresh-state behaviour of cementitious products: grading distribution, content of fines, quality of fines (through the sand equivalent test), density, water absorption and presence of sulphates and organic impurities. The content of impurities in the NA is negligible (sand equivalent: 91%, water-soluble sulphates below 1%, acid-soluble sulphates of class AS0.2 and total sulphur below 1%, light impurities below 0.1%). Since the composition of BA is well-known and controlled, sand equivalent and content of impurities were not tested. Table 2 presents densities, fines content and 24-h water absorption of the NA and BA. The fine content of the BA is well below 0.5% since the minimum particle size of 1 mm was imposed by sieving under controlled laboratory conditions.

Fig. 2 presents the particle size distribution of NA and BA. As expected, due to sieving BA exhibited a narrow grading range (1–2 mm), with over 90% of particles above the 1.0 mm sieve, while the NA, with size distribution 0–2 mm, exhibited 49% of its particles passing the 0.5 mm sieve.

The state-of-the-art commonly argues that recycled aggregates are rougher and more elongated than natural aggregates, especially when the natural aggregate is rounded gravel (as is this case) instead of a crushed aggregate. This will have consequences on the mix design and on the fresh and hardened state behaviour of the cementitious material.

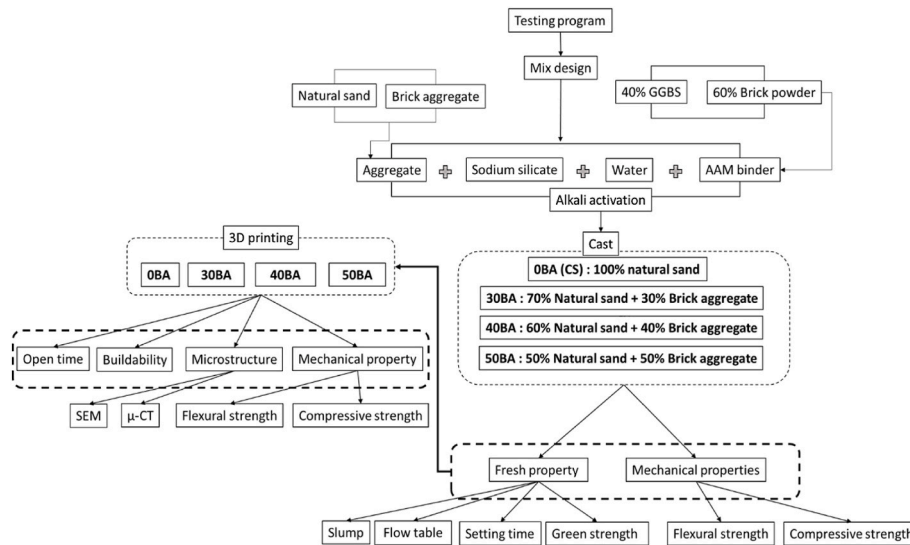


Fig. 1. Illustration of the experimental testing program.

Table 1

Oxide compositions of BP and GGBS obtained from XRF.

Material	SiO ₂	Al ₂ O ₃	CaO	Fe ₂ O ₃	MgO	K ₂ O	SO ₃	TiO ₂	Na ₂ O LOI
GGBS	27.55	9.06	48.91	0.69	7.23	0.36	2.37	0.45	0.34 1.2
BP	63.4	13.35	0.48	7.12	–	2.26	0.67	1.48	–2.9

Table 2

Physical properties of natural and recycled aggregates.

Property	Fines content	Bulk density [kg/m ³]	Relative particle density [kg/m ³]	Saturated surface-dry density [kg/m ³]	Oven-dry density [kg/m ³]	24h water absorption [%]
NA	<3%	1617	2633	2610	2597	0.53
BA	<0.5%	1130	2634	2330	2144	8.70

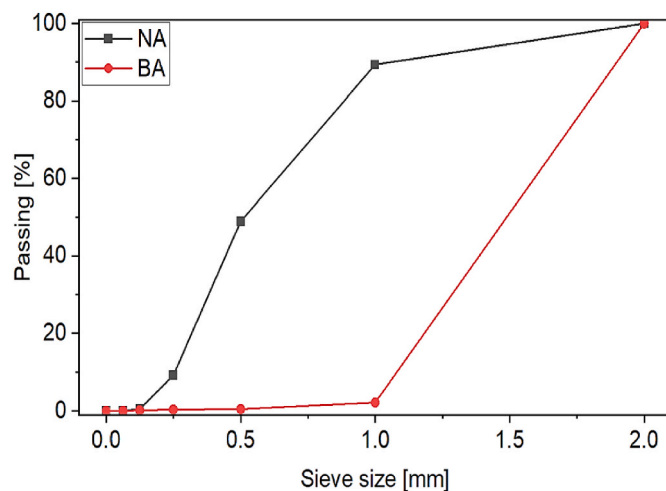


Fig. 2. Particle size distribution of NA and BA.

Elongated particles have been associated with higher water demand for the same workability, more micro-bleeding around the interface between aggregate and mortar and better flexural strength in comparison to rougher surface texture, while rougher texture particles are associated with higher viscosity, higher water demand and better interface between aggregates and particles (Mehta and Monteiro, 2014). Fig. 3

presents optical images of the NA and BA. The BA are elongated, while the NA are spherical, and the surface of the BA is much rougher than that of the NA.

2.2. Mix formulation, casting and 3D printing of specimens

The mix formulation of the four different 3D printable compositions prepared and investigated are given in Table 3. Based on the previous study conducted by Al-Noaimat et al. (Al-noaimat et al., 2023c), the optimum precursor developed, which corresponds to the best-performing mixture in their study, was selected to investigate its various printing properties. In all samples, the precursor content was kept constant and equal to 60% BP and 40% GGBS, with an aggregate-to-binder ratio of 1.2 and a water-to-binder ratio of 0.4, as shown in Table 3. The solid sodium metasilicate (Na₂SiO₃) activator (SS) with a constant content of 12% of the weight of the precursor was used for all mixtures. The replacement ratios of NA with BA were 30%, 40% and 50%-wt. (by weight). Most of the research on recycled aggregate concrete accounts for the water absorption of the RA (either the aggregates are saturated before use, which is not a feasible option for fine recycled aggregates, or the water absorbed by the BA is calculated and added to the mix (Pacheco et al., 2019)). In this paper, the water absorbed by the BA was not accounted for when defining the mix design (that is, the effective w/b ratio was not defined beforehand – e.g. by being imposed as equal to that of the mix without BA). This was deliberate since, as long as the concrete is properly extruded, any water absorbed would be beneficial to buildability and to the hardened state

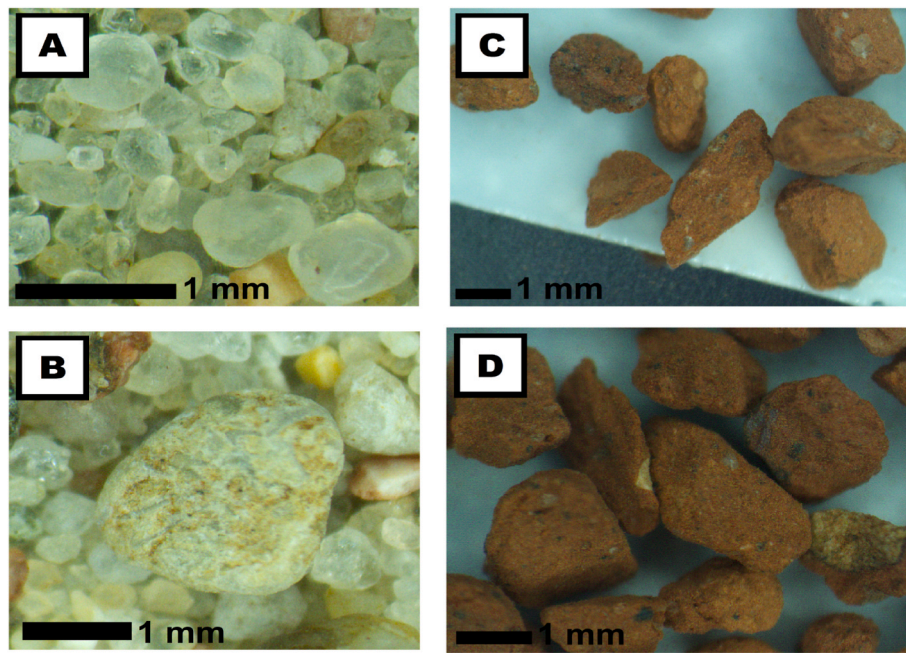


Fig. 3. Optical microscope images of (a–b) NA and (c,d) BA.

Table 3

Mix formulations of the different mixtures.

ID	BP (%)	GGBS (%)	Natural aggregate (%)	BA (%-wt.)	SS (%-wt.)	Total water (%-wt.)	Effective water (%-wt.)
OBA	60	40	100	0	12	0.4	0.394
30BA	60	40	70	30	12	0.4	0.37
40BA	60	40	60	40	12	0.4	0.36
50BA	60	40	50	50	12	0.4	0.35

properties of the mortar, improving its overall behaviour. Therefore, the following rationale was followed:

- The mix OBA was defined first;
- Mixes containing BA were produced with the same total water of the mix OBA;
- If the mixes were not extrudable or buildable or if any fresh state measurement deviated significantly from that of mix OBA, the water content was iteratively changed;
- After all mixes are defined, the effective water content was calculated by subtracting the water absorbed in the first 30 min after mixing, which was determined as 91% of the 24-h water absorption for the BA following the test protocol presented in (Rodrigues et al., 2013) and assumed as 100% of the 24-h water absorption for the NA due to the small water absorption of this aggregate;
- It was found that no adjustments to the total water were needed.

The mixtures were prepared in two stages. First, the dry ingredients, including precursor, aggregates, and activator, were inserted together into the mixer and dry-mixed for 3 min. Following dry-mixing, water was added gradually to the mixture while being mixed within a duration of 2 min and mixing continued for 8 min more (i.e., 10 min of wet-mixing in total). Ten min of mixing time was employed to ensure mixture homogeneity. The mixing procedure was conducted in control room conditions (20 °C and 40% RH) to ensure consistency. Following mixing, fresh mixtures were poured into prismatic polystyrene moulds with a dimension of 40 × 40 × 160 mm³ immediately for the conventional cast method or fed to the printer hopper. After casting or printing, specimens were oven-cured at ambient temperature until the test age.

2.3. Printing process

A three-axis gantry-type extrusion-based 3D printer was used in this study, illustrated in Fig. 4a. The extruder comprises (i) an auger connected to a three-axes rail system, moved and controlled by a computer program in the printer software. (ii) A hopper with a top opening of 185 mm, through which the materials were fed. (iii) A circular nozzle with an outlet diameter of the extruder of 25 mm. The extruder gage contains a maximum printing space with the length, width, and height of 1400, 1200, 800 mm, respectively. An illustration of the extruder and the printing process of one-part AAMs is presented in Fig. 4 b. The printing speed and nozzle standoff distance were 42 mm/s and 10 mm, respectively. A straight line with a cross-section of 40 × 40 mm² (See Fig. 4a) and immediately after extrusion, three prisms with a dimension of 40 × 40 × 160 mm³ were cut for each mixture.

3. Testing methods

3.1. Fresh properties

3.1.1. Workability and flow measurements of fresh mixture

Fresh properties can be related to two essential requirements of the 3D printable mixtures, which are pumpability and buildability. Previous studies have claimed that slump measurement can be related to the buildability and static yield stress of the mixtures, whereas slump flow can be linked to the dynamic yield stress and pumpability of the mixes (Tay et al., 2019). A flow table test was conducted to investigate the consistency and workability of the various mixtures according to the procedures described in BS EN 1015:3–1999 (BS EN 1015-3). The flow diameter was recorded on the fresh mixture at 0, 5, 10 and 15 min at the

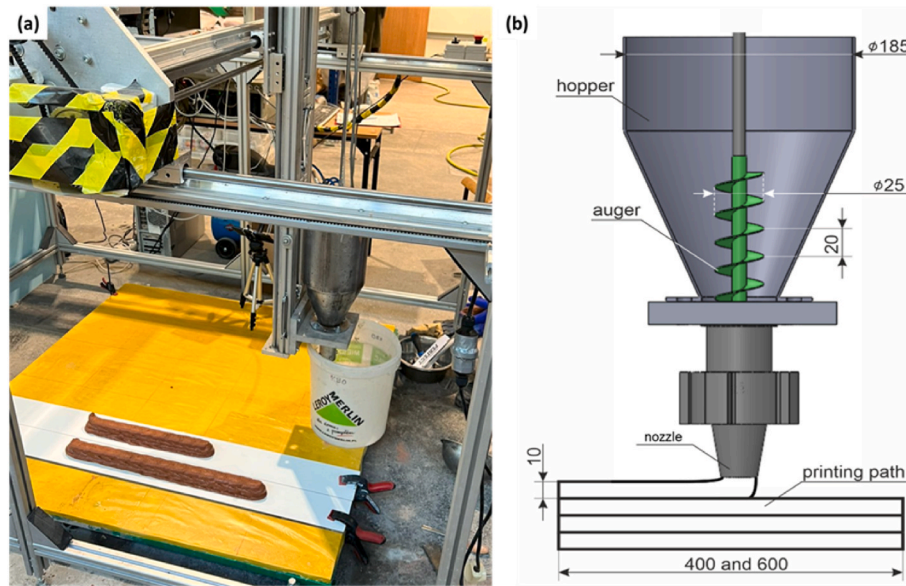


Fig. 4. (a) Extrusion-based 3D printer and (b) illustration of the extruder parts.

end of the mixing process. The flowability percentage was calculated using the following equation (Eq. (1)):

$$\text{Flowability (\%)} = \left(\frac{d_{\text{average}} - d_0}{d_0} \right) \times 100 \quad (\text{Eq.1})$$

where, d_{average} is the average spread diameter of AAM mortar in two perpendicular directions, and d_0 is the bottom (large) diameter of the cone.

A mini-slump test was also assessed to determine the workability of the fresh AAM following BS EN 12350-2:2009 (BS EN 12350-2, 2009). Mini-slump cone apparatus was used with a height, top and bottom diameter of 50, 70 and 100 mm, respectively. The slump value was recorded, directly after the end of the mixing process, as the flow height reduction after 1 min of pouring the fresh mixture into the cone. Furthermore, the relative slump value (Γ_p) was measured following the ASTM C-1437 (ASTM C1437-01, 2001) using the following equation (Eq. 2):

$$\Gamma_p = \left(\frac{d}{d_0} \right)^2 - 1 \quad (\text{Eq.2})$$

where d is the average spread diameter of the mixture in two perpendicular directions spread and d_0 is the bottom cone-diameter.

3.1.2. Setting time

The setting time is one of the key factors that affect the production of 3D printed concrete since a short setting time would result in the hardening and blockage of the mixture in the extruder. Therefore, the initial setting time of the one-part AAM mortars was determined immediately after the mixing process finished. The fresh mixture was poured into the cone, and a Vicat apparatus was used to record the setting time of the mixtures following BS EN 480-2:2006 (BS EN 480) and ASTM C191-08 (ASTM C191-08, 2008). A cone with a height, top and bottom diameter of 40, 70 and 80 mm, respectively, was used. The Vicat needle penetration was recorded every 5 min until a four mm needle penetration depth was reached.

3.1.3. Open time

Open time, also known as printability window, refers to the period during which the freshly prepared material paste demonstrates adequate workability for printing. Various studies estimated the open time of the fresh pastes using Vicat, slump, or rheology tests at predetermined

intervals (Le et al., 2012; Bos et al., 2016; Ma et al., 2018a). In this study, the open time was assessed by printing simple lines of 150 mm × 26 mm, having a resting time of 5 min until the printed line showed discontinuity.

3.1.4. Green strength

The “green” strength of the AAM specimen was conducted by the uniaxial unconfined compressive test (UUCT) and digital image correlation (DIC) system (GOM ARAMIS). The test was performed on a small compression test stand (Fig. 5). The stand has installed force sensor with a range of up to 500 N (HBM C9C 0.5 kN) coupled to an HBM MGC Plus AB22A bridge. A loading rate of 15 mm/min was assumed for the performed test. Tests were conducted on the cylindrical specimens ($d = 60$ mm, $h = 120$ mm), 30 min after water contact. Mix preparation and tests were made in a laboratory condition at temperature $20^\circ (\pm 2^\circ)$ and relative humidity of $RH = 55\% (\pm 5\%)$. For each type of sample, four specimens were tested. A similar test approach for green strength evaluation has been used by other authors (Skibicki et al., 2022; Panda et al., 2019a; Wolfs et al., 2018; Ding et al., 2020; Casagrande et al., 2020). In addition, the compressive test device was equipped with LVDT sensor to control the displacement of the specimen. The deformation of the specimen during the compression test was recorded by DIC system, which controlled the displacements of 9 markers placed on the specimen. During the test, results from the force sensor were recorded by DIC system via an analogue connector. The system configuration between HBM MGC Plus AB22A and GOM ARAMIS allows for full analysis of force-strain relationships in GOM Correlate software. Fig. 5a shows the test stand for UUCT with ARAMIS system test.

Similar mixing procedures were used to prepare the fresh mixture with the difference that the samples were moulded in plastic cylindrical form with a diameter of 60 mm and height of 120 mm. Before starting the test, the specimen was demoulded, set up on the bench and 9 markers were placed on the specimen surface (Fig. 5b).

3.2. Mechanical properties

Flexural strength using a three-point bending test setup and compressive strength tests were conducted on cast and 3D printed samples cured for three days following BS EN 196-1 (BS EN 196-1, 2016). For assessing the mechanical anisotropic behaviour of the printed samples, the tests were conducted on cut prisms from the printed samples in lateral (v) and perpendicular (h) directions to the printing

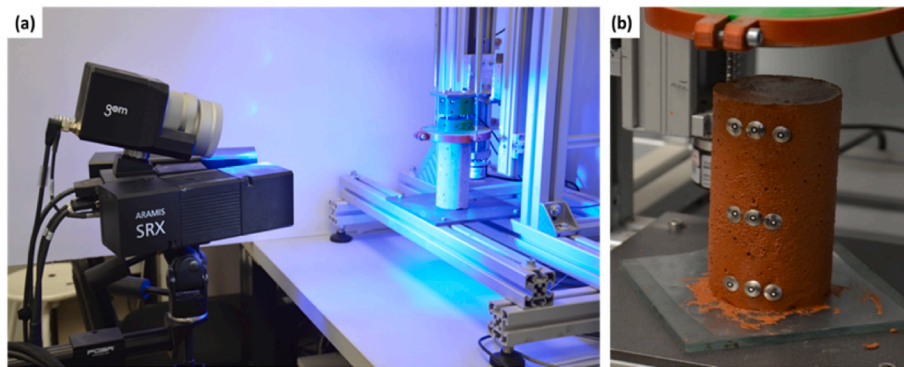


Fig. 5. (a) Test stand for UUCT with ARAMIS and (b) demoulded specimen before the test.

path, as shown in Fig. 6. The cast samples were prepared with a dimension of $40 \times 40 \times 160 \text{ mm}^3$, and the printed samples were cut to have similar dimensions. To ensure accurate measurements, the printed samples were polished using sand paper to smoothen the surface and the dimensions of the polished samples were measured prior to testing, as shown in Fig. 6a. The tests on both printed and cast samples were conducted using a load rate of 1 mm/min on a Universal Testing System (Instron 5960). The density of the prisms was recorded prior to the flexural strength test. The flexural and compressive strength results were calculated as the average of three samples and six halves, respectively, and the standard deviation of the different samples was measured and reported as error bars.

3.3. Microstructure analysis

A scanning electron microscope (SEM) was used to investigate the microstructure of the different one-part AAM 3D printed samples. The analysis was conducted on a sliced sample cut from the printed specimens with a dimension of 8 mm^3 using Supra 35VP, Carl Zeiss, Germany. To prevent surface charging effects, the samples were gold coated for a period of 3 min using an Edwards S150B sputter coater. An accelerating voltage of 5 kV was used to capture around 10 secondary electron images from each sample to ensure meaningful observation on a working distance (WD) of 25–29 mm. In addition to utilising SEM, X-ray micro-computed tomography (micro-CT) was employed for non-destructive

investigation of the volumetric microstructural characteristics of the printed materials. Through micro-CT scanning, a series of cross-sectional images were acquired, as depicted in the second image of Fig. 7. The primary focus of employing micro-CT was to examine the pore characteristics, which involved segmenting the pore regions using the modified Otsu method. The resulting binarized images were then stacked to generate a 3D volumetric representation of the pore volume, as illustrated in Fig. 7. In this study, a micro-CT image resolution of $22.12 \mu\text{m}/\text{pixel}$ was used, which proved sufficient for capturing both micro and macro pores that can impact the physical and mechanical properties of the materials. For the investigation, samples were scanned with enough height to include the interlayers of the printed samples. The pore structures of the printed samples were analysed using the micro-CT data obtained.

3.4. Buildability

The buildability of the different samples was investigated following ad hoc testing method through 3D printing cylindrical structures with a diameter of 150 mm using 5500 g of fresh mixture. The same printing parameters of mechanical properties assessment were utilised for this test. For buildability, one batch of materials was prepared for each mixture, and the printing was continuing until failure or material finishes. The quality of the printed cylinders was investigated visually in terms of vertical distortion, maximum height, and layer deformation. The buildability and outer-surface finish of the different mixtures were investigated on high-quality pictures. The maximum height of each printed samples and the reduction at the bottom layers was measured using Image software to allow for accurate and meaningful measurements.

4. Results and discussions

4.1. Effect of brick aggregate on one-part AAM fresh properties

4.1.1. Flowability and slump measurements

The most critical parameter to anticipate successful 3D printing of cementitious-based materials is their fresh properties. The fresh properties of AAM, including flowability, shape stability and workability, is significantly affected by the characteristics of the aggregate, such as surface texture, volume fraction, size and gradation (Bhowmick and Ghosh, 2012). The flowability percentage and slump measurements of each mixture are presented in Fig. 8. As shown in Fig. 8a, the results indicated that the flowability of all mixtures diminished when BA was used to partially replace NA. The maximum reduction was registered for the samples with 50% substitution of natural aggregates, in which the flowability decreased from 65% for 0BA to 48% for 50BA. Similarly, both relative slump value and slump height decreased as the incorporation ratio of the BA increased, as shown in Fig. 8b. This behaviour is

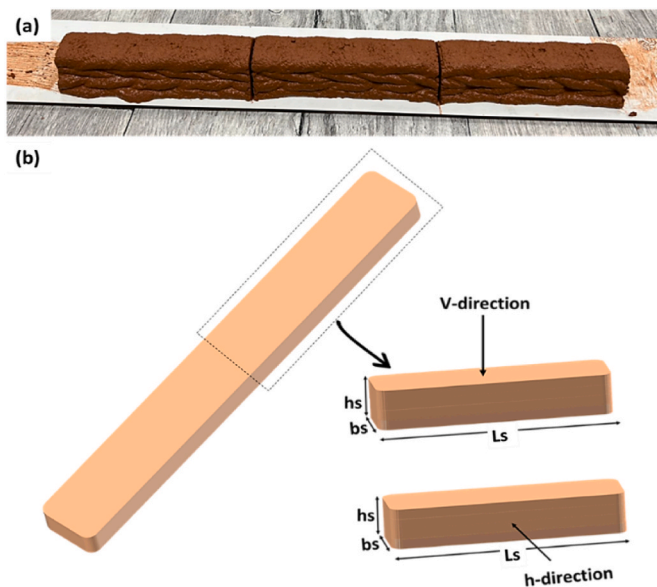


Fig. 6. (a) 3D printed line cut into prismatic samples for mechanical properties and (b) illustration of loading directions.

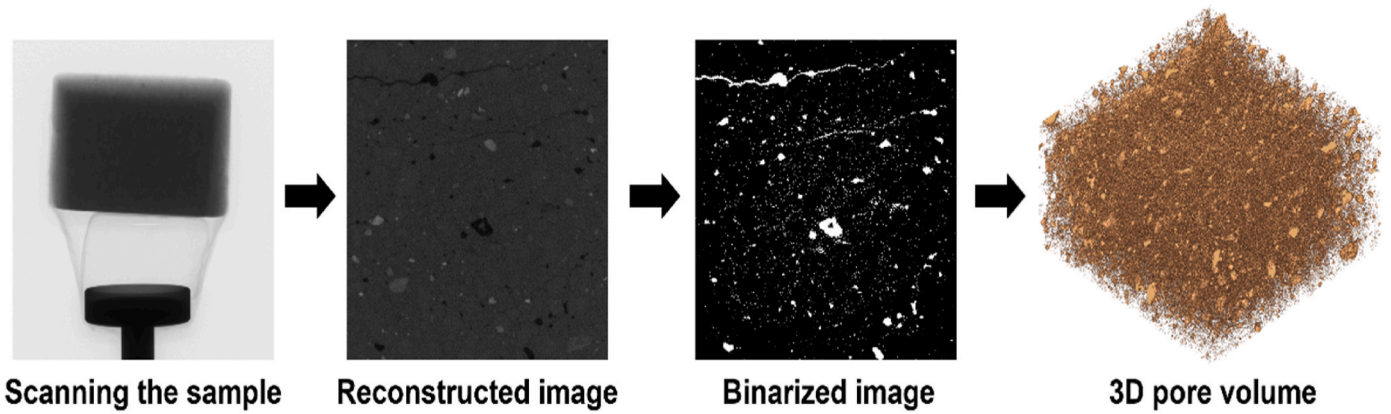


Fig. 7. Micro-CT imaging to segment the pore volume (Note: in the binarized image, the white represents the pore part within the specimen.).

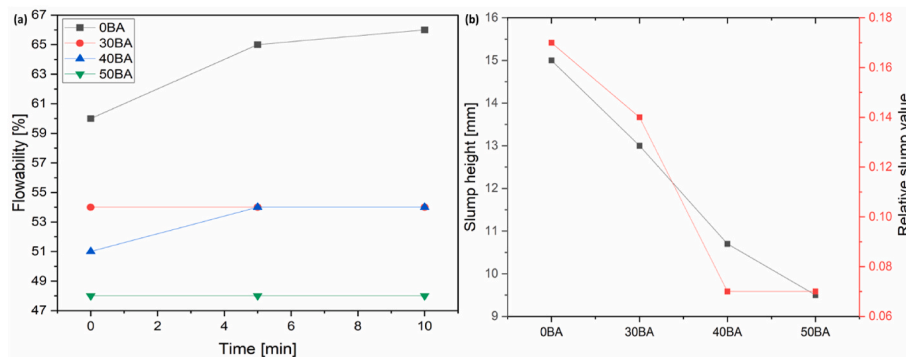


Fig. 8. Fresh properties of one-part AAMs with different BA content: (a) flowability as function of time and (b) slump height.

due to geometry and roughness of the BA and the option of not accounting for the water absorbed by the BA when defining the mixes (see Section 2.2). There are four types of water in the fresh mixture, which are (i) adsorbed water on the particle surface, (ii) free water, (iii) water filling the gaps between the particles (Hou et al., 2021), and (iv) water absorbed by the BA, which is relevant due to its large water absorption. The fluidity of the mixture is influenced only by the free water when the mixture’s overall water content is constant. Since the total water of the mix was fixed, this means that the amount of free water decreases when BA are used due to its high water absorption capacity. It is important to note that BA particles have a rough and elongated shape that can significantly hamper the workability and flowability of mixtures. This is due to the increased friction between components, which is not a concern for NA particles with a spherical and round shape. The slump height suggests that the mixtures with BA may have excellent shape retention and buildability. However, the flowability loss can result in difficulties in extruding the mixtures and might lead to a blockage in the extrusion system during printing. These aspects are discussed in the next section.

4.1.2. Green strength

The green strength has been evaluated based on DIC system. The green compressive strength [kPa] was calculated according to Eq. (3).

$$\sigma(\epsilon) = \frac{N(\epsilon)}{A(\epsilon)} \tag{Eq.3}$$

Where $N(\epsilon)$ is the force in N measured by HBM C9C 0.5 kN force sensor, $A(\epsilon)$ is the area measured by DIC system. During the test, the specimen diameter was measured automatically by the DIC system using markers placed on the sample. The ARAMIS device allows to precisely determine the green compressive stress (σ) – strain (ϵ) curves for each mix, as

presented on Fig. 9. The maximum compressive stress (σ_{max}) and Young’s modulus are reported in Table 4. The Young’s modulus was calculated according to Eq. (4) for the linear part of stress – strain curve between strains $\epsilon_u = 0.06$ and $\epsilon_d = 0.04$. For all obtained data, the values of coefficient of variation (CoV) were calculated.

$$E = \frac{\sigma_{0.06} - \sigma_{0.04}}{\epsilon_u - \epsilon_d} \tag{Eq.4}$$

where:

$\sigma_{0.04}$ and $\sigma_{0.06}$ are the compressive stress for strains equal to 0.04 and 0.06, respectively.

Fig. 10 shows the failure mechanism of the examined specimens. The photos were obtained by GOM Corelate 2022 ARAMIS software. Despite

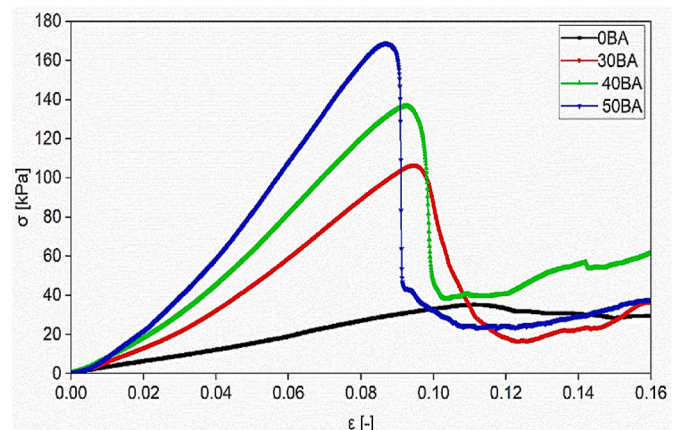


Fig. 9. Stress-strain relationship for tested specimens.

Table 4
Comparison of the maximum compressive stresses and Young's modulus.

Mix	BA replacement ratio [%-wt.]	σ_{max} [kPa]	CoV [%]	$\varepsilon(\sigma_{max})$ [-]	E [kPa]	CoV [%]
0BA	0	35.16	9.79	0.111	341.48	6.11
30BA	30	106.28	4.49	0.095	1334.25	9.47
40BA	40	136.46	8.91	0.093	1828.51	7.48
50BA	50	168.69	6.15	0.087	2465.31	7.29

the addition of brick aggregates (BA), the failure pattern was unaffected. The specimens showed a shear failure pattern, which was evident from the visible diagonal shear crack on each specimen. Moreover, it is important to mention that the lateral deformation decreases with the increase of the percentage of BA added because the BA content affects the directional dependency of the pores, which is attributed to the mechanical behaviour of the specimens.

Fig. 11 shows the relationship between maximum green compressive stresses (σ_{max}), green Young's modulus and the BA incorporation. The data has been analysed by linear regressions. The results show a linear relationship between the incorporation ratio of the BA and the mechanical properties. The σ_{max} increased with increasing the BA content in mix ($R^2 = 0.99$, see Fig. 11). The mixes with 30%, 40% and 50% of brick aggregate (BA) content had σ_{max} increase of 202.2%, 288.1% and 379.7%, respectively. The Young's modulus value increased with the addition of BA, with a linear regression ($R^2 = 0.98$). The mixes with 30%, 40% and 50% BA content had increased Young's modulus by 290.7%, 435.5% and 622.0%, respectively. Increasing BA content significantly increased the green mechanical properties of AAM mixes (up to 379.7% for compressive strength σ_{max} , up to 622.0% for Young Modulus). The failure pattern was similar for all BA content.

Nevertheless, the lateral deformation decreased with the BA content.

Several studies have proposed different methods to define the fresh properties of the cementitious mixtures, some of which, for example rheology tests, are unable to fully evaluate the mix properties for 3D printing applications due to test specifications. Recently, a more realistic fresh property test, i.e., the green strength test, has been widely used as a practical tool to anticipate the shape retention and buildability of cementitious composites. However, for alkali-activated materials, further research is needed to assess the data on green strength (Pasupathy et al., 2023; Zhong and Zhang, 2022; Bong SH et al., 2022a; Kondepudi et al., 2022; Dai et al., 2023; Kondepudi and Subramaniam, 2021; Kawashima et al., 2013; Jones et al., 2019). The maximum green strength value of 35.16 kPa was registered for the reference mix (0BA), similar value (i.e., 34.84 kPa) was obtained in a study conducted by Casagrande et al. (2020). However, the incorporation of BA gradually increased the green strength to 106.28 kPa, 136.46 kPa, and 168.69 kPa for 30BA, 40BA, and 50BA, respectively. Research on incorporating waste brick aggregate on the fresh performance of cement-based or AAM mixes is limited (Pasupathy et al., 2023; Christen et al., 2022a, 2022b). The remarkable increase in the green strength of the mixtures containing BA can be associated with the early-age strengthening phenomenon caused by the incorporation of BA. This has been proven in several research in which the incorporation of BA results in a considerable reduction in the slump values (Christen et al., 2022a, 2022b). Moreover, according to Pasupathy et al. (2023), the inclusion of ground brick waste results in a substantial enhancement in the static yield stress. Their results indicated that the aforementioned static yield stress enhancement is due to the high water absorption capacity of the brick waste present in the composition, which ultimately diminishes the mixture's ball-bearing ability. The increase in green strength and Young's modulus observed in the present paper are a natural

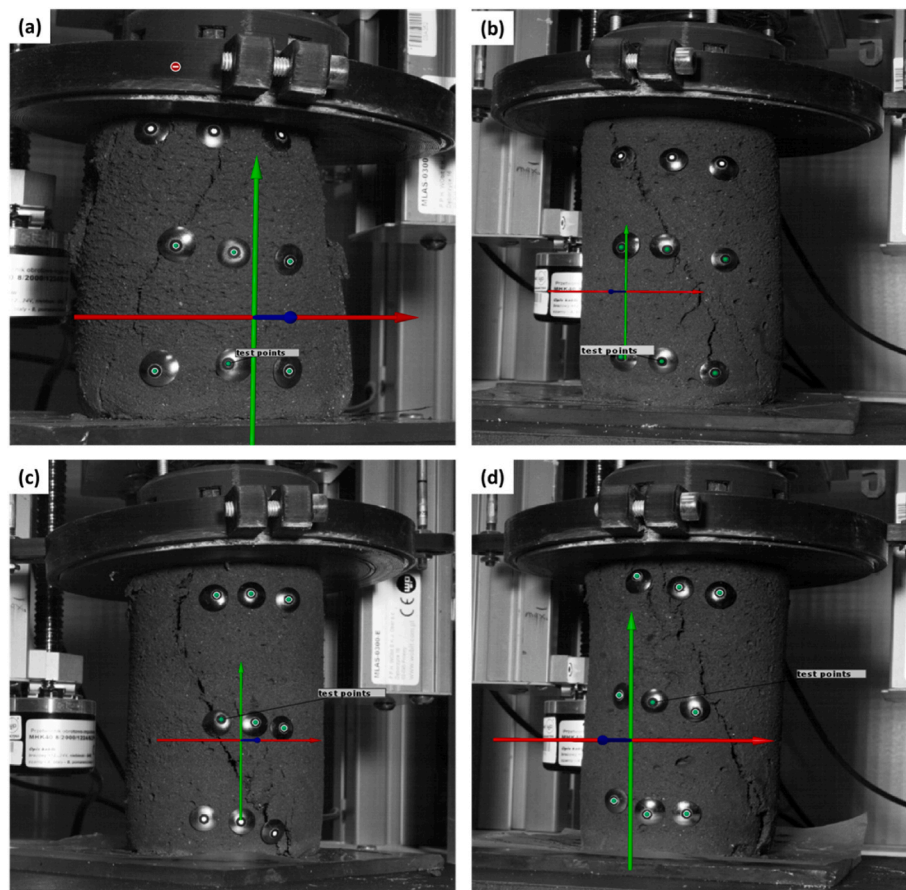


Fig. 10. Failure mechanism of the specimens (recorded by ARAMIS system): (a) 0BA; (b) 30BA; (c) 40BA; (d) 50BA

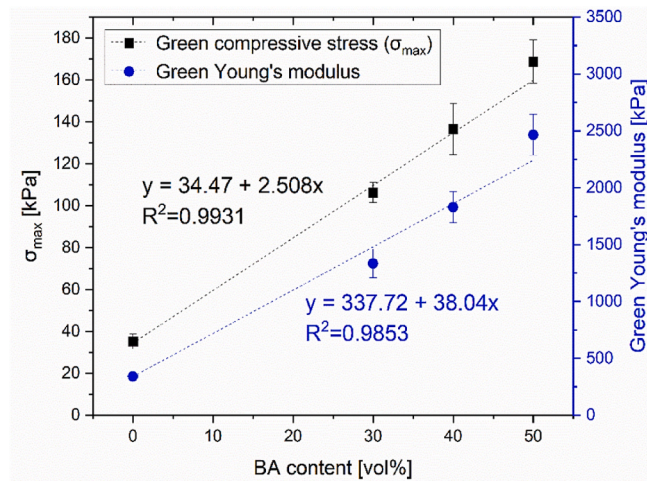


Fig. 11. Relationship between the BA content and the maximum green strength and green Young modulus. (For interpretation of the references to colour in this figure legend, the reader is referred to the Web version of this article.)

consequence of using a rough and porous aggregate with high water absorption capacity, particularly at early ages (7.9% at 30 min), and not compensating this water absorption in the mix design. In line with the green strength results, the green Young modulus of the mixtures gradually increased from 341.48 kPa for the reference mix (OBA) and reached 1334.25 kPa, 1828.51 kPa, and 2465.31 kPa, for the 30BA, 40BA, and 50BA, respectively. It's worth noting that previous studies reported green Young modulus values ranging from 27.92 kPa (Ding et al., 2020) to 488 kPa (Casagrande et al., 2020), which is broadly dependant on the mix formulation specifications. Achieving high values of green mechanical properties is a good indication of the mixtures' improved buildability (as discussed in section 4.4). However, it is worth noting that the high water absorption of the recycled aggregate used and the nature of alkali-activated materials lead to a remarkably decreased open time (see section 4.1.3).

4.1.3. Setting and open time

Different studies reported a direct relationship between the initial setting time and the open time of cement-based materials (Le et al., 2012; Panda et al., 2019b), which is essential for large-scale 3D printing process (Elyamany et al., 2018). In this study, the impact of different BA content on the initial setting time and open time of the AAM mixtures were investigated and the results are presented in Fig. 12. Similar to the

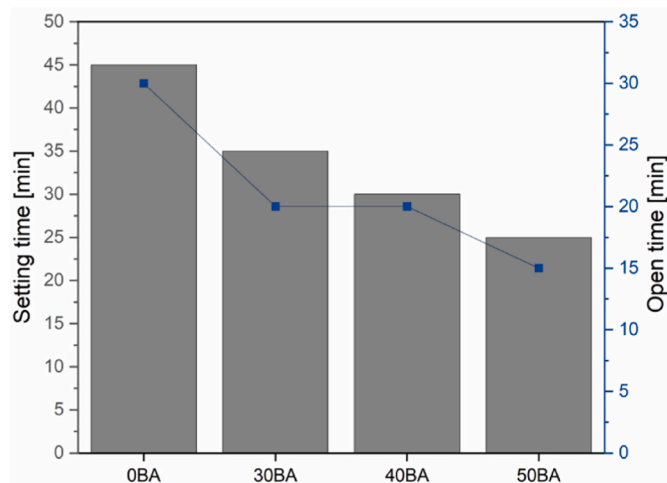


Fig. 12. Setting and open time of the mixtures with different BA content.

flowability and slump measurements, the setting and open times were shortened when incorporating BA. It can be seen that increasing BA content from 0% to 50% gradually decreased the setting time from 45 min for OBA to 35 min, 30 min, and 25 min for 30BA, 40BA, and 50BA, respectively. A similar trend was observed for the open time, in which the extrusion open time values decreased from 30 min for OBA to 15 min for 50BA. This behaviour is mostly caused by the water absorption over time of the brick aggregates, which decreased the amount of free water in the mixture, decreasing the particles flocculation. That, in turn, resulted in a drier mixture, increasing the pressure required for the needle to penetrate and for the layer to be extruded for the open time. These results are in good agreement with the results obtained in flowability and slump measurements (see Fig. 8) and with the green strength results.

4.2. Mechanical properties

Fig. 13 shows the flexural and compressive strength and the oven-dry density of cast and 3D printed one-part AAM with and without BA. As per previous investigations, the printed samples are expected to exhibit anisotropic mechanical behaviour due to the formation of voids between the successive layers (Ma et al., 2018b; Sikora et al., 2022). Accordingly, the flexural and compressive strength of the 3D printed specimens were measured in lateral (h) and perpendicular (v) directions to the printing path to investigate the anisotropic behaviour (Fig. 5b). Both flexural and compressive strength results increased with increasing BA content without noticeable differences in the oven-dry density of the samples. Fig. 13a shows that incorporating BA enhanced the flexural performance of the mixtures. The 50BA sample exhibited the highest performance for both cast and 3D printed samples regardless of the loading direction, which exhibited around 41%, 47%, and 24% higher flexural strength for the 50BA cast specimen, as well as printed samples in lateral and perpendicular directions, respectively, compared to their corresponding values for OBA. Similarly, compressive strength results gradually increased with increasing BA content. The highest compressive strength performance was achieved by 50BA, where the compressive strength was increased by 18%, 39%, and 38% for the cast specimen, lateral (h-direction) and perpendicular (v-direction) directions, respectively, compared to OBA, as shown in Fig. 13b. As in the case of green strength, the higher strength values with increasing BA content could be due to the lower amount of water in the system, confirmed from the workability results in Section 3.1.1. This can result in better compactness and fine microstructure of the mixtures. According to the authors' previous study (Al-noaimat et al., 2023c), incorporating BA decreased the dominant peak pore size distribution, reflecting the denser microstructure in the presence of BA. It is generally known for cementitious-based materials that the denser the mixture, the higher the strength (Jiang et al., 2020). Another reason could be BA's rough, irregular surface and porous structure that enhances the adhesion between the matrix and aggregate particles (see Fig. 14). This was confirmed by SEM images, which showed the satisfactory embedment of BA in the matrix and the good interlocking between the matrix and the aggregate (see Fig. 14). When exposed to external loading, the good interlocking and adhesion of the binder paste with BA allowed for efficient stress transmission, increasing the overall mechanical performance (Lo et al., 2016). The flexural strength results of the different 3D printed mixtures depend on the testing directions, where 3D printed samples exhibited lower strength when applying the load in perpendicular (v-direction) direction to the printing path compared to both cast and lateral direction (h-direction), as shown in Fig. 13a. Applying the load perpendicularly (v-direction) to the printing path showed relatively higher and comparable results to the cast sample. Similar directional behaviour was obtained for compressive strength, as shown in Fig. 13b. However, regardless of the loading direction, the 3D printed samples exhibited higher compressive strength values than the cast specimen. According to Nerella et al. (2019), there are two types of compaction used for printed

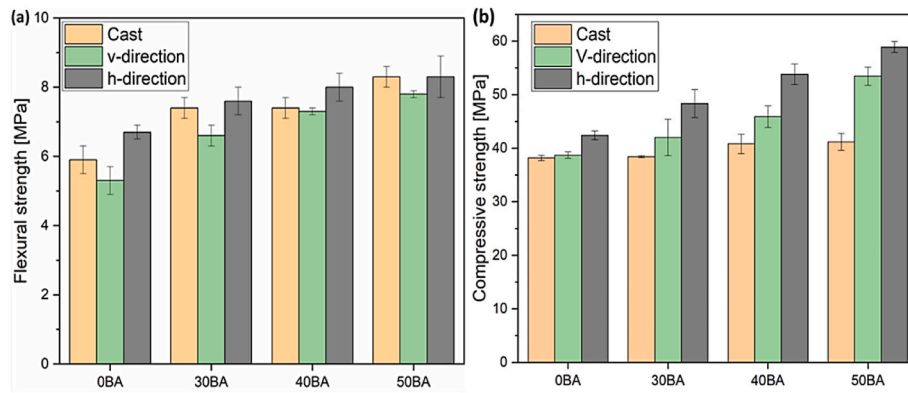


Fig. 13. (a) Flexural strength and (b) compressive strength of cast and 3D printed brick-based one-part AAM containing different brick aggregate (BA) percentages. Error bars presents the standard deviation.

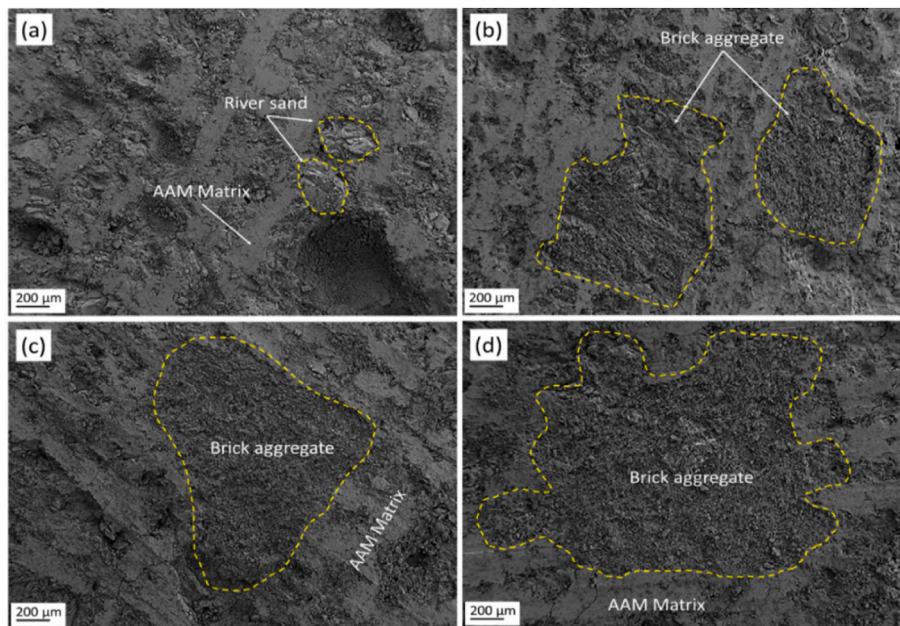


Fig. 14. SEM images obtained from samples extracted from the printed lines of (a) 0BA, (b) 30BA, (c) 40BA and (d) 50BA

structures, which are extrusion and weight compaction of deposited layers. The high level of compaction during printing leads to production of samples with less porosity and denser structures, ultimately improving mechanical performance compared to that of conventional cast method. The compressive strength of the printed samples was also dependent on the testing direction, where applying load lateral (h-direction) to the printing direction showed higher strength values than the perpendicular direction (v-direction) for the different mixtures. A similar anisotropic mechanical behaviour was observed in previous studies (Pasupathy et al., 2023; Panda et al., 2019c; Muthukrishnan et al., 2021; Bong SH et al., 2022b; Bong SH et al., 2021). Those studies investigated the mechanical performance of 3D printed samples in three directions, which are longitudinal, perpendicular and lateral to the printing path. The findings of those studies were contradictory, in which some reported the highest strength when the load was applied in longitudinal direction, followed by lateral, and finally perpendicularly to the printing path (Pasupathy et al., 2023; Panda et al., 2019a; Bong SH et al., 2022b), conflicting the findings of the presented study. On the other hand, similar findings to this study are reported by other researchers, i.e., showing that printed samples exhibited the highest strength performance in the lateral direction (Muthukrishnan et al., 2021; Bong SH et al., 2021). According to Panda et al. (2017),

mimicking micro-mechanics of mixtures' material can explain this mechanical anisotropic behaviour, where applying load laterally to the printed filament allows for the uniform distribution of load throughout the cross-section. However, in the case of applying load in a transverse direction, the beads start to separate from each other, lowering the specimens' strength. Hence, this anisotropic behaviour could be due to the difference in compaction between the directions, indicating that the self-weight of the material was insufficient to compact the filaments properly and resulted in lower performance perpendicular to the printing direction (see section 4.3). The high strength observed in the lateral direction (h-direction) can be because of the better interlocking induced by the layer deposition pattern, in which the rotational movement of the auger in the extrusion system causes an upward twisting in the deposited filaments (see Fig. 6a), increasing the contact area and the interlocking between the deposited and subsequent layer, which allows for the uniform distribution of load on the cross-section of the sample. Thus, enhancing the ability of the printed samples to withstand loads and increasing their strength performance.

4.3. X-ray micro-computed tomography

The micro-CT technique was employed to investigate the

microstructural characteristics of the printed materials. Specifically, the samples designated as 0BA, 30BA, 40BA, and 50BA were analysed to explore the influence of different mixtures on the material properties, particularly with regard to pores. In the x, y, and z directions, a volume of $1000 \times 1000 \times 500$ voxels was examined for each composition. Fig. 15 presents the pore volume for each specimen. Only pores larger than the pixel size used ($22.12 \mu\text{m}$) were considered, resulting in calculated porosity values of 3.2%, 3.8%, 3.7%, and 5.4% for the 0BA, 30BA, 40BA, and 50BA samples, respectively. These porosity values indicate that there are no significant differences in porosity among the samples based on the amount of BA contents, although 50BA sample shows slightly larger porosity than other cases. To conduct a more comprehensive analysis, several aspects of pore structures were examined. Fig. 16a illustrates the distribution of pore sizes in the printed specimens. It can be seen that 0BA sample exhibited a more uniformity and homogeneity pore structure sizes that those containing BA. This finding suggests that an increase in BA content results in the production of specimens containing pores within a specific size range. Fig. 16b displays the spatial distribution of the pores throughout the height of the specimen. Despite the slightly larger overall porosity observed in the 50BA samples, this figure reveals that the local porosity values are generally consistent, indicating a uniform pore structure quality in the printed samples.

The micro-CT data was also utilised to investigate the effect of BA on pore shape. Fig. 17 presents the sphericity of pores based on their size and the relative solid density of the samples. Sphericity serves as an indicator for particle shape, where a sphericity value of 1 indicates a perfect sphere, and lower values indicate increasing anisotropy. Fig. 17a demonstrates that the reference sample (0BA) contains more isotropic pores compared to samples with BA content. Among the BA samples, no significant variation was observed based on the BA amount; however, an increase in BA content correlated with a higher degree of anisotropy. This suggests that the quantity of BA affects pore structures, including shape, potentially influencing the mechanical properties of printed materials (Sikora et al., 2022). Those results could explain the directional anisotropic mechanical behaviour of the 3D printed samples, especially for 50BA sample. The pore shape of 50BA indicated a relatively high pore anisotropy than other samples, which can explain the high variance between the lateral and perpendicular testing directions in compressive strength results of 50BA (see section 4.2). Besides pore characteristics, the micro-CT data can be utilised to analyse the relative

solid density of the samples. The grayscale values in the reconstructed micro-CT images indicate the relative solid density, where higher grayscale values correspond to a denser phase. Fig. 17b illustrates the average pixel values at different specimen heights. The figure suggests that, overall, the measured relative solid densities appear to be uniform, although there is a slight increase in density with higher amounts of BA contents. To summarise, the micro-CT data enables effective examination of pore and solid characteristics of the materials based on their BA contents.

4.4. Buildability

Fig. 18 presents the printed cylinders of 5500 g of the different mixtures for the buildability test. The buildability test was executed through continuous printing until a failure was observed. Following printing, the maximum printing height of each cylinder was also measured. It can be seen that mixtures prepared with BA exhibited better buildability than the control mixture. As shown in Fig. 18a, the control mixture could be printed up to nine layers before collapse. However, layer deposition was terminated due to the excessive deformation in the bottom layer, which leads to structural instability and failure if further layers were deposited. The behaviour of the control sample was predicted from slump height and green strength results, which showed a high reduction in height without applying any load, and low green strength, indicating that the mixture does not have enough stiffness to sustain the weight of the successive layers. Replacing natural aggregate with BA enhanced the buildability, where 30BA and 40BA exhibited good buildability performance, reaching 13 layers and exhibiting an experimental height of 123 mm and 125 mm (see Fig. 18 b and c), respectively, which is comparable to the theoretically designed height of 130 mm. It is noteworthy that the number of layers deposited stopped at 13 layers not because this was the buildability threshold of the mixtures, but because the fixed amount of materials (i.e., 5500 g) did not allow any more printing. Hence, more than 13 layers could have been printed without showing any deformation or collapse. Moreover, increasing the BA content to 50% reached 13 layers without showing any deformation in the bottom layers or collapse (see Fig. 18d), having almost similar experimental height (i.e., 129 mm) to the theoretical designated height (130 mm). However, it can be seen that a discontinuity started to occur at the 12th layer, indicating the finish of the

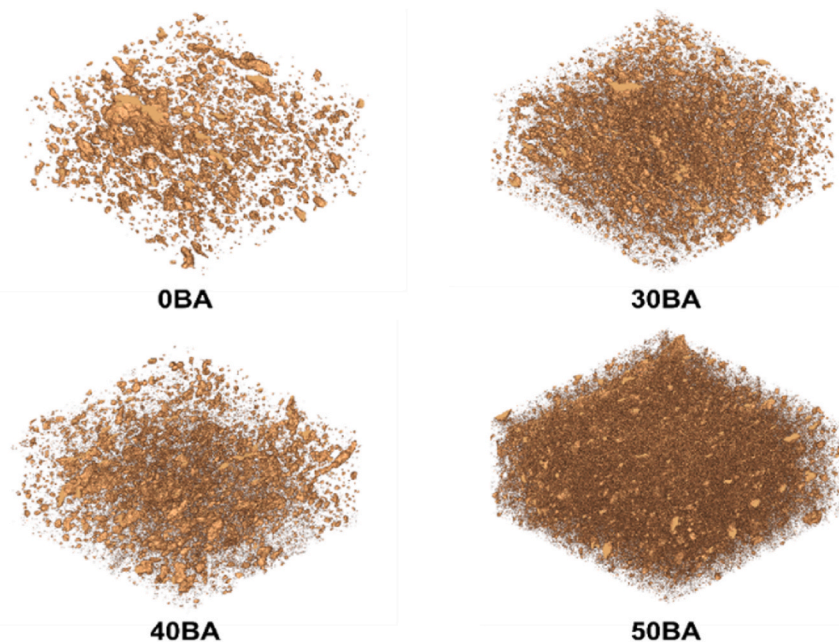


Fig. 15. Pore volume image of each specimen.

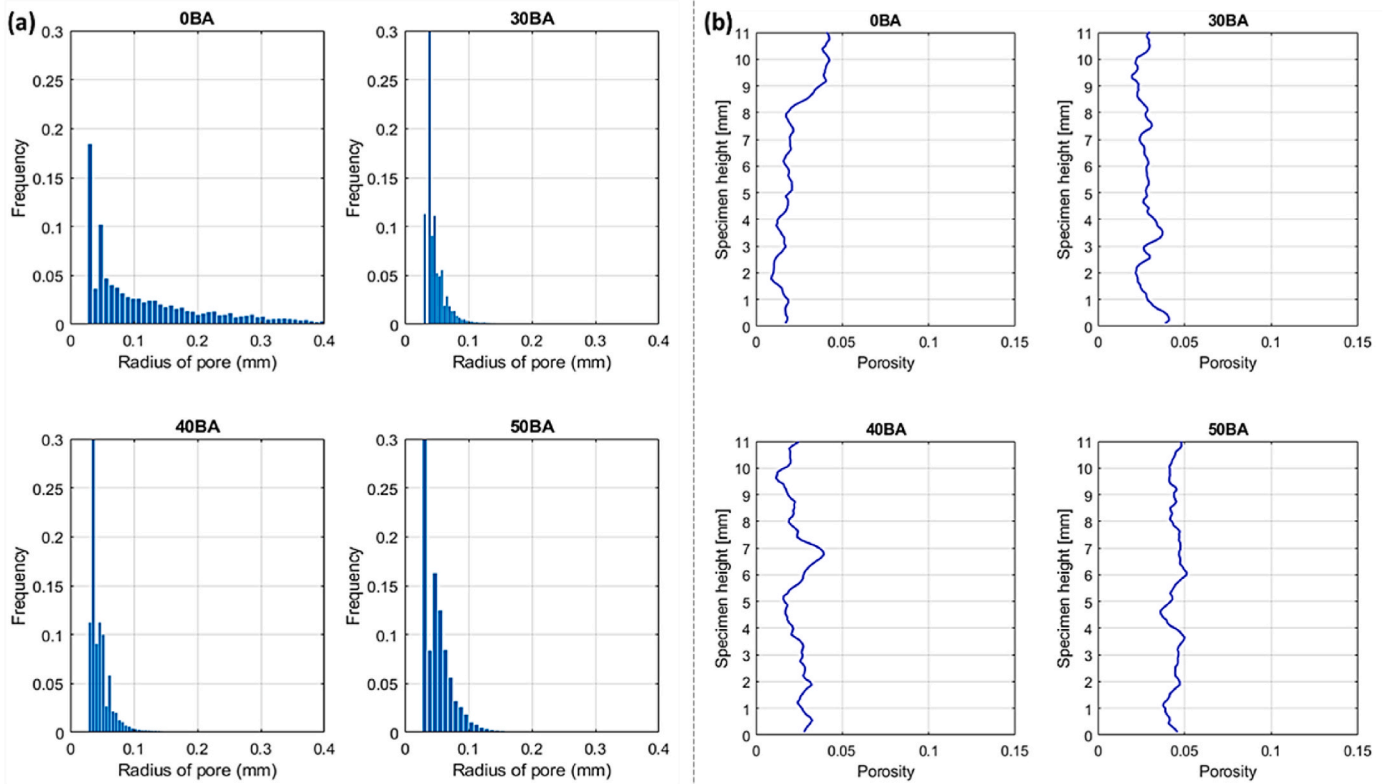


Fig. 16. (a) Pore size distribution of the specimens and (b) the spatial porosity according to the specimen height in each specimen.

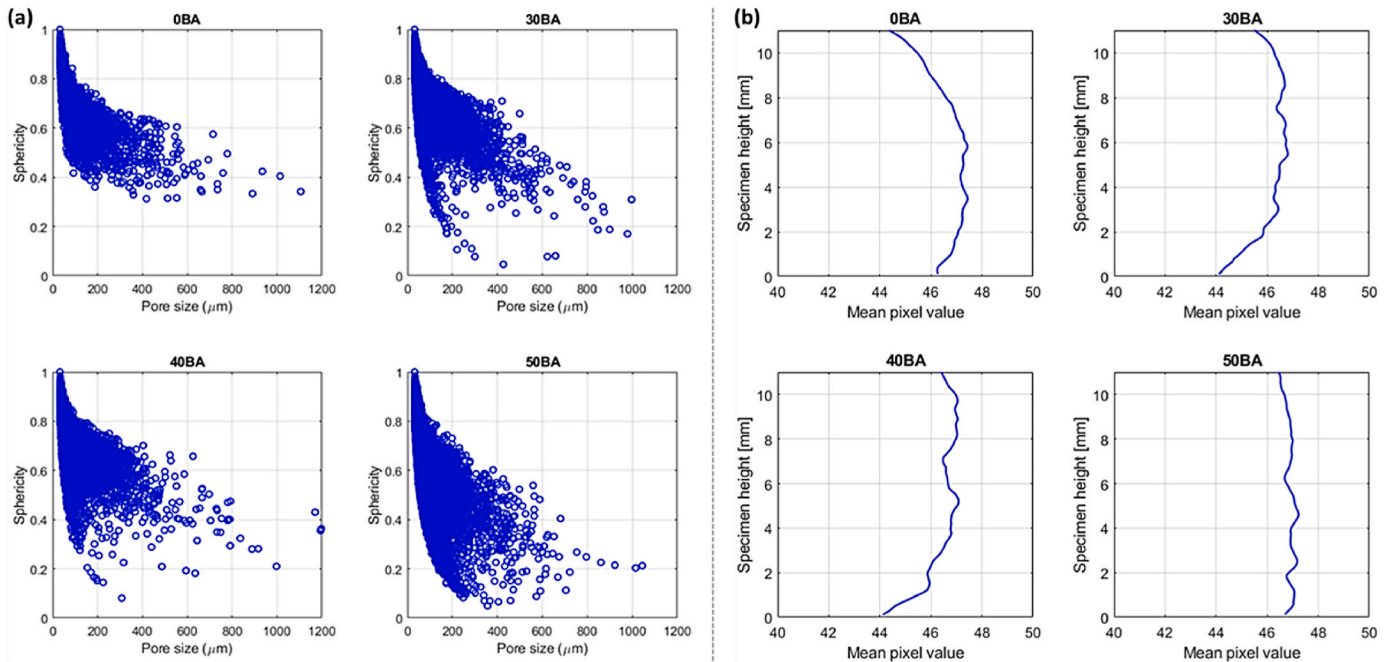


Fig. 17. (a) Sphericity of each specimen according to the pore sizes and (b) Relative solid density along the specimen height (Note: the mean pixel value of the micro-CT image indicates the relative density of the solid phase.).

materials. As mentioned in section 3.1.1, pumpability and dynamic yield stress can be evaluated through flowability, while buildability and static yield stress can be measured through slump measurement. Thus, it can be indicated that the greater the BA content, the higher the static yield stress and the better the buildability of the mixture. That could explain the excellent shape retention without showing noticeable radial

distortion with increasing BA content (i.e., 40BA and 50BA) compared to 30BA. The excellent buildability of mixtures with BA confirms the feasibility of utilising end-of-life brick in aggregate form in the concrete 3D printing application to promote recycling construction and demolition waste.

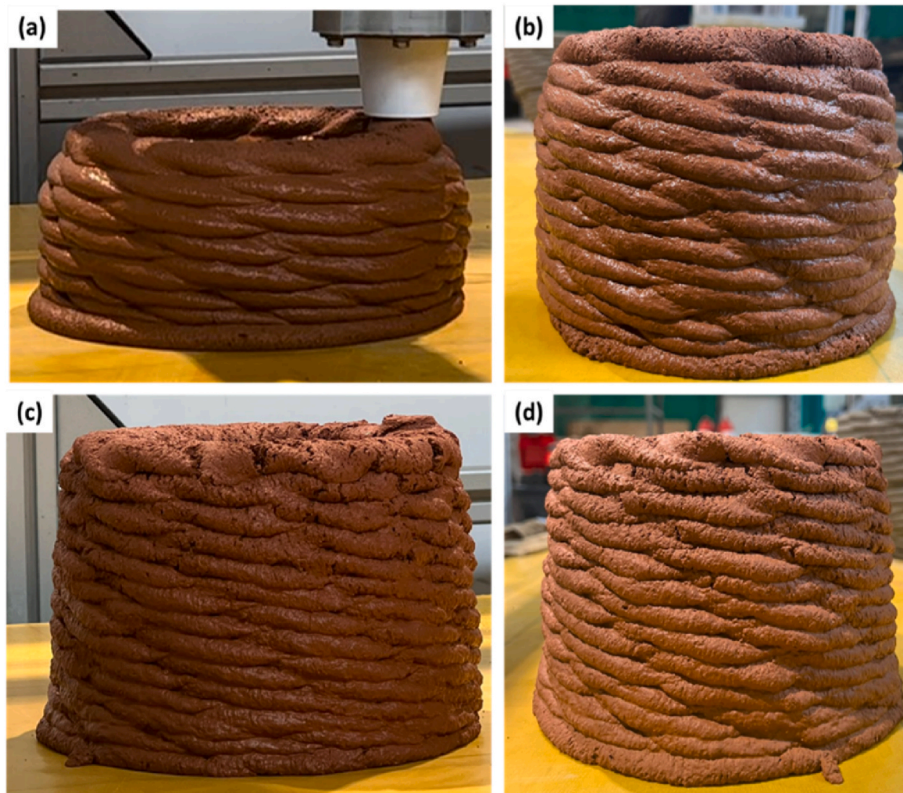


Fig. 18. Buildability of the different 3D printed one-part AAM: (a) 0BA, (b) 30BA, (c) 40BA, and (d) 50BA.

5. Conclusions

This study investigated the feasibility of recovering end-of-life bricks in a powder physical state as a binder as well as 1–2 mm particles as a natural aggregate replacement to develop one-part alkali-activated materials for 3D printing applications. Recycled brick aggregate was incorporated with different percentages in the AAM mixtures comprised of 60% brick dust and 40% GGBS as binder, and their impact on fresh properties, which determines the mixture's printability, was evaluated. Hardened properties and buildability of the different mixtures were also evaluated. According to the results, the following conclusion can be made:

- 1) Incorporating brick aggregate decreased the slump measurements and height, flowability and setting time while increasing the green strength and green Young's modulus. This could be due to the high water absorption of brick aggregates and decrease in the ball-bearing effect when replacing the spherical and round shape natural aggregate with the irregular brick particles.
- 2) Flexural and compressive strength increased with increasing brick aggregate content for both cast and printed specimens. Printed samples showed anisotropic mechanical behaviour, having the highest flexural and compressive strength performance when the load was applied laterally to the printing direction (h-direction) compared to both the cast sample and the perpendicular direction.
- 3) Flexural strength of the printed specimens had comparable strength values to cast when the load was applied perpendicular (v-direction) to the printing path. In contrast, the printed samples' compressive strength was higher than the cast mixture.
- 4) Micro-CT results indicated that incorporating brick aggregates led to having comparable porosity and solid density between the different contents and the mixture with natural sand while increased the anisotropy of the pore structure. However, increasing brick aggregate content to 50% increased the calculated porosity of the mixture.

Moreover, the pore shape also found to be dependent on brick aggregate content, where 50% replacement level showed the highest degree of anisotropy, which could be the reason of the directional anisotropic behaviour of the mixtures under compression and flexural strength tests.

- 5) Replacing natural aggregate with brick aggregate improved the buildability of the mixtures, exhibiting a higher number of layers without showing any failure compared to the control mixture, which showed a high deformation in the bottom layer. However, increasing brick aggregate content to 50% resulted in a discontinuity after depositing 12 layers.

This work proves the suitability and compatibility of using brick aggregate form as an alternative to the limited natural aggregate. However, this research indicated a limited setting time of the mixtures due to not considering the water being absorbed by recycled aggregate particles. Hence, further research is required on the presented methodology (i.e., not considering compensating the absorbed water), which negatively impacted extrudability while improving the buildability of the mixtures. Furthermore, investigations on the impact of adding the absorbed water on the different properties of alkali-activated materials, which might impair the buildability of the mixture while extending the setting and extrusion time can be interesting. The buildability in this study was limited to one batch since the work was conducted on a lab scale. Therefore, the buildability of the mixture containing brick aggregate with and without superplasticiser is worth investigations.

Funding

This work was funded as part of the DigiMat project, which has received funding from the European Union's Horizon 2020 research and innovation program under the Marie Skłodowska-Curie grant agreement ID: 101029471.

This research was funded in part by the National Center for Research

and Development (NCBR), Poland within Project no. ERA-MIN3/140/Recycl3D/2022 (ERA-NET Cofund ERA-MIN3 (Joint Call 2021)). The funding provided by FCT - the Portuguese Foundation for Science and Technology, is acknowledged: references UIDB/04625/2020 (CERIS research centre) and ERA-MIN3/0001/2021 (ERA-NET Cofund ERA-MIN3).

Declaration of competing interest

The authors declare that they have no known competing financial interests or personal relationships that could have appeared to influence the work reported in this paper.

Data availability

Data will be made available on request.

Acknowledgements

Authors would like to thank Ms. Valentine Kurgat (IEASTE student at WPUTS) for support with laboratory work.

References

- BS EN 1015-3: Methods of Test for Mortar for Masonry- Part 3: Determination of Consistency of Fresh Mortar (by flow table), 1999. n.d..
- Adaloudis, M., Bonnin Roca, J., 2021. Sustainability tradeoffs in the adoption of 3D Concrete Printing in the construction industry. *J. Clean. Prod.* 307, 127201 <https://doi.org/10.1016/j.jclepro.2021.127201>.
- Adesanya, E., Ohehoja, K., Luukkonen, T., Kinnunen, P., Illikainen, M., 2018. One-part geopolymer cement from slag and pretreated paper sludge. *J. Clean. Prod.* 185, 168–175. <https://doi.org/10.1016/j.jclepro.2018.03.007>.
- Agusti-Juan, I., Müller, F., Hack, N., Wangler, T., Habert, G., 2017. Potential benefits of digital fabrication for complex structures: environmental assessment of a robotically fabricated concrete wall. *J. Clean. Prod.* 154, 330–340. <https://doi.org/10.1016/j.jclepro.2017.04.002>.
- Al-noaimat, Y.A., Akis, T., 2023. Influence of cement replacement by calcinated kaolinitic and montmorillonite clays on the properties of mortars. *Arabian J. Sci. Eng.* <https://doi.org/10.1007/s13369-023-08041-y>.
- Al-noaimat, Y.A., Hamidreza, S., Chougan, M., Al-kheetan, M.J., 2023a. A review of 3D printing low-carbon concrete with one-part geopolymer : engineering , environmental and economic feasibility. *Case Stud. Constr. Mater.* 18, e01818 <https://doi.org/10.1016/j.cscm.2022.e01818>.
- Al-noaimat, Y.A., Chougan, M., Al-kheetan, M.J., Al-mandhari, O., Al-saidi, W., Al-maqbali, M., et al., 2023b. 3D printing of limestone-calcined clay cement : a review of its potential implementation in the construction industry. *Results Eng.* 18, 101115 <https://doi.org/10.1016/j.rineng.2023.101115>.
- Al-noaimat, Y.A., Chougan, M., Al-kheetan, M.J., Yio, M.H.N., Wong, H.S., Hamidreza, S., 2023c. Upcycling end-of-life bricks in high-performance one-part alkali-activated materials. *Dev. Built Environ.* 16, 100231 <https://doi.org/10.1016/j.dibe.2023.100231>.
- Allahverdi, A., Kani, E.N., 2013. In: Use of Construction and Demolition Waste (CDW) for Alkali-Activated or Geopolymer Cements. Woodhead Publishing Limited. <https://doi.org/10.1533/9780857096906.3.439>.
- ASTM C1437-01, 2001. Standard test method for flow of hydraulic cement mortar. Standard 7–8.
- ASTM C191-08, 2008. Standard Test Method for Normal Consistency and Setting Time of Hydraulic Cement.
- Bhowmick, A., Ghosh, S., 2012. Effect of synthesizing parameters on workability and compressive strength of Fly ash based Geopolymer mortar. *Int. J. Struct. Civ. Eng.* 3, 168–177. <https://doi.org/10.6088/ijcser.201203013016>.
- Bong SH, Xia, M., Nematollahi, B., Shi, C., 2021. Ambient temperature cured 'just-add-water' geopolymer for 3D concrete printing applications. *Cem. Concr. Compos.* 121, 104060 <https://doi.org/10.1016/j.cemconcomp.2021.104060>.
- Bong SH, Nematollahi, B., Nerella, V.N., Mechtcherine, V., 2022a. Method of formulating 3D-printable strain-hardening alkali-activated composites for additive construction. *Cem. Concr. Compos.* 134, 104780 <https://doi.org/10.1016/j.cemconcomp.2022.104780>.
- Bong SH, Nematollahi, B., Xia, M., Ghaffar, S.H., Pan, J., Dai, J.G., 2022b. Properties of additively manufactured geopolymer incorporating mineral wollastonite microfibers. *Construct. Build. Mater.* 331, 127282 <https://doi.org/10.1016/j.conbuildmat.2022.127282>.
- Bos, F., Wolfs, R., Ahmed, Z., Salet, T., 2016. Additive manufacturing of concrete in construction: potentials and challenges of 3D concrete printing. *Virtual Phys. Prototyp.* 11, 209–225. <https://doi.org/10.1080/17452759.2016.1209867>.
- BS EN 12350-2, 2009. Testing Fresh Concrete-Part, vol. 2. Slump-test n.d.
- BS EN 12620, 2013. Aggregates for Concrete.
- BS EN 196-1, 2016. Methods of Testing Cement - Part 1: Determination of Cement n.d.
- BS EN 480: Admixtures for Concrete, Mortar and Grout-Test Methods-Part 2: Determination of Setting Time-2006 n.d..
- Casagrande, L., Esposito, L., Menna, C., Asprone, D., Auricchio, F., 2020. Effect of testing procedures on buildability properties of 3D-printable concrete. *Construct. Build. Mater.* 245, 118286 <https://doi.org/10.1016/j.conbuildmat.2020.118286>.
- Charkhtab Moghaddam, S., Madandoust, R., Jamshidi, M., Nikbin, I.M., 2021. Mechanical properties of fly ash-based geopolymer concrete with crumb rubber and steel fiber under ambient and sulfuric acid conditions. *Construct. Build. Mater.* 281, 122571 <https://doi.org/10.1016/j.conbuildmat.2021.122571>.
- Chen, Y., Jia, L., Liu, C., Zhang, Z., Ma, L., Chen, C., et al., 2022. Mechanical anisotropy evolution of 3D-printed alkali-activated materials with different GGBFS/FA combinations. *J. Build. Eng.* 50, 104126 <https://doi.org/10.1016/j.jobe.2022.104126>.
- Chougan, M., Hamidreza, S., Nematollahi, B., Sikora, P., Dorn, T., Stephan, D., et al., 2022. Effect of natural and calcined halloysite clay minerals as low-cost additives on the performance of 3D-printed alkali-activated materials. *Mater. Des.* 223, 111183 <https://doi.org/10.1016/j.matdes.2022.111183>.
- Christen, H., Cho, S., van Zijl, G., de Villiers, W., 2022a. Phase change material infused recycled brick aggregate in 3D printed concrete. *Heliyon* 8, e11598. <https://doi.org/10.1016/j.heliyon.2022.e11598>.
- Christen, H., van Zijl, G., de Villiers, W., 2022b. The incorporation of recycled brick aggregate in 3D printed concrete. *Clean Mater* 4, 100090. <https://doi.org/10.1016/j.clema.2022.100090>.
- Dadsetan, S., Siad, H., Lachemi, M., Sahmaran, M., 2019. Construction and demolition waste in geopolymer concrete technology: a review. *Mag. Concr. Res.* 71, 1232–1252. <https://doi.org/10.1680/jmacr.18.00307>.
- Dai, X., Tao, Y., Van Tittelboom, K., De Schutter, G., 2023. Rheological and mechanical properties of 3D printable alkali-activated slag mixtures with addition of nano clay. *Cem. Concr. Compos.* 139, 104995 <https://doi.org/10.1016/j.cemconcomp.2023.104995>.
- Dang, J., Zhao, J., Hu, W., Du, Z., Gao, D., 2018. Properties of mortar with waste clay bricks as fine aggregate. *Construct. Build. Mater.* 166, 898–907. <https://doi.org/10.1016/j.conbuildmat.2018.01.109>.
- Ding, T., Xiao, J., Qin, F., Duan, Z., 2020. Mechanical behavior of 3D printed mortar with recycled sand at early ages. *Construct. Build. Mater.* 248, 118654 <https://doi.org/10.1016/j.conbuildmat.2020.118654>.
- El-gamal, S.M.A., El-hosiny, F.I., Amin, M.S., Sayed, D.G., 2017. Ceramic waste as an efficient material for enhancing the fire resistance and mechanical properties of hardened Portland cement pastes. *Construct. Build. Mater.* 154, 1062–1078. <https://doi.org/10.1016/j.conbuildmat.2017.08.040>.
- El-seidy, E., Chougan, M., Sambucci, M., Al-kheetan, M.J., Biblioteca, I., Valente, M., et al., 2023. Lightweight alkali-activated materials and ordinary Portland cement composites using recycled polyvinyl chloride and waste glass aggregates to fully replace natural sand. *Construct. Build. Mater.* 368, 130399 <https://doi.org/10.1016/j.conbuildmat.2023.130399>.
- Elyamany, H.E., Abd Elmoaty, A.E.M., Elshaboury, A.M., 2018. Setting time and 7-day strength of geopolymer mortar with various binders. *Construct. Build. Mater.* 187, 974–983. <https://doi.org/10.1016/j.conbuildmat.2018.08.025>.
- Farhan, N.A., Sheikh, M.N., Hadi, M.N.S., 2019. Investigation of engineering properties of normal and high strength fly ash based geopolymer and alkali-activated slag concrete compared to ordinary Portland cement concrete. *Construct. Build. Mater.* 196, 26–42. <https://doi.org/10.1016/j.conbuildmat.2018.11.083>.
- Fatta, D., Papadopoulos, A., Avramikos, E., Sgourou, E., Moustakas, K., Kourmoussis, F., et al., 2003. Generation and Management of Construction and Demolition Waste in Greece — an Existing Challenge, vol. 40, pp. 81–91. [https://doi.org/10.1016/S0921-3449\(03\)00035-1](https://doi.org/10.1016/S0921-3449(03)00035-1).
- Hou, P., Ronald, T., Li, Q., Chen, H., Kawashima, S., Sui, T., et al., 2021. Mechanisms dominating thixotropy in limestone calcined clay cement (LC3). *Cement Concr. Res.* 140, 106316 <https://doi.org/10.1016/j.cemconres.2020.106316>.
- Hwang, C., Damtie, M., Vo, D., Huynh, T., 2019. Development of high-strength alkali-activated pastes containing high volumes of waste brick and ceramic powders. *Construct. Build. Mater.* 218, 519–529. <https://doi.org/10.1016/j.conbuildmat.2019.05.143>.
- Ican, H., Sahin, O., Kul, A., Yildirim, G., Sahmaran, M., 2022. Rheological properties and compressive strength of construction and demolition waste-based geopolymer mortars for 3D-Printing. *Construct. Build. Mater.* 328, 127114 <https://doi.org/10.1016/j.conbuildmat.2022.127114>.
- Jiang, X., Zhang, Y., Xiao, R., Polaczyk, P., Zhang, M., Hu, W., et al., 2020. A comparative study on geopolymers synthesized by different classes of fly ash after exposure to elevated temperatures. *J. Clean. Prod.* 270, 122500 <https://doi.org/10.1016/j.jclepro.2020.122500>.
- Jones, S.Z., Bentz, D.P., Martys, N.S., George, W.L., Thomas, A., 2019. Rheological Control of 3D Printable Cement Paste and Mortars, vol. 19. Springer International Publishing. https://doi.org/10.1007/978-3-319-99519-9_7.
- Kawashima, S., Chaouche, M., Corr, D.J., Shah, S.P., 2013. Rate of thixotropic rebuilding of cement pastes modified with highly purified attapulgite clays. *Cement Concr. Res.* 53, 112–118. <https://doi.org/10.1016/j.cemconres.2013.05.019>.
- Kondepudi, K., Subramaniam, K.V.L., 2021. Formulation of alkali-activated fly ash-slag binders for 3D concrete printing. *Cem. Concr. Compos.* 119 <https://doi.org/10.1016/j.cemconcomp.2021.103983>.
- Kondepudi, K., Subramaniam, K.V.L., Nematollahi, B., Bong SH, Sanjayan, J., 2022. Study of particle packing and paste rheology in alkali activated mixtures to meet the rheology demands of 3D Concrete Printing. *Cem. Concr. Compos.* 131, 104581 <https://doi.org/10.1016/j.cemconcomp.2022.104581>.

- Le, T.T., Austin, S.A., Lim, S., Buswell, R.A., Gibb, A.G.F., Thorpe, T., 2012. Mix Design and Fresh Properties for High-Performance Printing Concrete, vols. 1221–32. <https://doi.org/10.1617/s11527-012-9828-z>.
- Lo, T.Y., Cui, H., Memon, S.A., Noguchi, T., 2016. Manufacturing of sintered lightweight aggregate using high-carbon fly ash and its effect on the mechanical properties and microstructure of concrete. *J. Clean. Prod.* 112, 753–762. <https://doi.org/10.1016/j.jclepro.2015.07.001>.
- Lu, W., 2019. Big data analytics to identify illegal construction waste dumping: a Hong Kong study. *Resour. Conserv. Recycl.* 141, 264–272. <https://doi.org/10.1016/j.resconrec.2018.10.039>.
- Luukkonen, T., Abdollahnejad, Z., Yliniemi, J., Kinnunen, P., Illikainen, M., 2018a. Comparison of alkali and silica sources in one-part alkali-activated blast furnace slag mortar. *J. Clean. Prod.* 187, 171–179. <https://doi.org/10.1016/j.jclepro.2018.03.202>.
- Luukkonen, T., Abdollahnejad, Z., Yliniemi, J., Kinnunen, P., Illikainen, M., 2018b. One-part alkali-activated materials: a review. *Cement Concr. Res.* 103, 21–34. <https://doi.org/10.1016/j.cemconres.2017.10.001>.
- Ma, G., Li, Z., Wang, L., 2018a. Printable properties of cementitious material containing copper tailings for extrusion based 3D printing. *Construct. Build. Mater.* 162, 613–627. <https://doi.org/10.1016/j.conbuildmat.2017.12.051>.
- Ma, G., Zhang, J., Wang, L., Li, Z., Sun, J., 2018b. Mechanical characterization of 3D printed anisotropic cementitious material by the electromechanical transducer. *Smart Mater. Struct.* 27 <https://doi.org/10.1088/1361-665X/aac789>.
- Markin, V., Krause, M., Otto, J., Schröfl, C., Mechtcherine, V., 2021. 3D-printing with foam concrete: from material design and testing to application and sustainability. *J. Build. Eng.* 43 <https://doi.org/10.1016/j.jobe.2021.102870>.
- Mehta, P.K., Monteiro, P.J.M., 2014. *Concrete: Microstructure, Properties, and Materials*. McGraw-Hill Education.
- Menna, C., Mata-falcón, J., Bos, F.P., Vantighem, G., Ferrara, L., Asprone, D., et al., 2020. Opportunities and challenges for structural engineering of digitally fabricated concrete. *Cement Concr. Res.* 133, 106079 <https://doi.org/10.1016/j.cemconres.2020.106079>.
- Migunthanna, J., Rajeev, P., 2022. Waste clay bricks as a geopolymer binder for pavement construction. *Sustainability* 14, 6456.
- Migunthanna, J., Rajeev, P., Sanjayana, J., 2021. Investigation of waste clay brick as partial replacement of geopolymer binders for rigid pavement application. *Construct. Build. Mater.* 305, 124787 <https://doi.org/10.1016/j.conbuildmat.2021.124787>.
- Muthukrishnan, S., Ramakrishnan, S., Sanjayana, J., 2021. Effect of alkali reactions on the rheology of one-part 3D printable geopolymer concrete. *Cem. Concr. Compos.* 116, 103899 <https://doi.org/10.1016/j.cemconcomp.2020.103899>.
- Nerella, V.N., Hempel, S., Mechtcherine, V., 2019. Effects of layer-interface properties on mechanical performance of concrete elements produced by extrusion-based 3D-printing. *Construct. Build. Mater.* 205, 586–601. <https://doi.org/10.1016/j.conbuildmat.2019.01.235>.
- Oikonou, N.D., 2005. Recycled concrete aggregates. *Cement Concr. Compos.* 27, 315–318. <https://doi.org/10.1016/j.cemconcomp.2004.02.020>.
- Ouda, A.S., Gharieb, M., 2020. Development of brick geopolymer pastes using concrete waste incorporating dolomite aggregate. *J. Build. Eng.* 27, 100919 <https://doi.org/10.1016/j.jobe.2019.100919>.
- Pacheco, J., de Brito, J., Chastre, C., Evangelista, L., 2019. Experimental investigation on the variability of the main mechanical properties of concrete produced with coarse recycled concrete aggregates. *Construct. Build. Mater.* 201, 110–120. <https://doi.org/10.1016/j.conbuildmat.2018.12.200>.
- Panda, B., Paul, S.C., Hui, L.J., Tay, Y.W.D., Tan, M.J., 2017. Additive manufacturing of geopolymer for sustainable built environment. *J. Clean. Prod.* 167, 281–288. <https://doi.org/10.1016/j.jclepro.2017.08.165>.
- Panda, B., Lim, J.H., Tan, M.J., 2019a. Mechanical properties and deformation behaviour of early age concrete in the context of digital construction. *Compos Part B* 165, 563–571. <https://doi.org/10.1016/j.compositesb.2019.02.040>.
- Panda, B., Unluer, C., Tan, M.J., 2019b. Extrusion and rheology characterization of geopolymer nanocomposites used in 3D printing. *Compos Part B Eng* 176, 107290. <https://doi.org/10.1016/j.compositesb.2019.107290>.
- Panda, B., Singh, G.B., Unluer, C., Tan, M.J., 2019c. Synthesis and characterization of one-part geopolymers for extrusion based 3D concrete printing. *J. Clean. Prod.* 220, 610–619. <https://doi.org/10.1016/j.jclepro.2019.02.185>.
- Pasupathy, K., Ramakrishnan, S., Sanjayana, J., 2023. 3D concrete printing of eco-friendly geopolymer containing brick waste. *Cem. Concr. Compos.* 138, 104943 <https://doi.org/10.1016/j.cemconcomp.2023.104943>.
- Paul, S.C., Babafemi, A.J., Anggraini, V., Rahman, M.M., 2018. Properties of normal and recycled brick aggregates for production of medium range (25–30 MPa) structural strength concrete. *Buildings* 8. <https://doi.org/10.3390/BUILDINGS8050072>.
- Puertas, F., García-díaz, I., Barba, A., Gazulla, M.F., Palacios, M., Gómez, M.P., et al., 2008. Ceramic wastes as alternative raw materials for Portland cement clinker production. *Cem. Concr. Compos.* 30, 798–805. <https://doi.org/10.1016/j.cemconcomp.2008.06.003>.
- Reig, L., Tashima, M.M., Borrachero, M.V., Monzó, J., Cheeseman, C.R., Payá, J., 2013. Properties and microstructure of alkali-activated red clay brick waste. *Construct. Build. Mater.* 43, 98–106. <https://doi.org/10.1016/j.conbuildmat.2013.01.031>.
- Robayo, R.A., Mulford, A., Munera, J., Mejía de Gutiérrez, R., 2016. Alternative cements based on alkali-activated red clay brick waste. *Construct. Build. Mater.* 128, 163–169. <https://doi.org/10.1016/j.conbuildmat.2016.10.023>.
- Rodrigues, F., Evangelista, L., Britoa, J De, 2013. A new method to determine the density and water absorption of fine recycled aggregates. *Mater. Res.* 16, 1045–1051. <https://doi.org/10.1590/S1516-14392013005000074>.
- Sikora, P., Techman, M., Federowicz, K., El-Khayatt, A.M., Saudi, H.A., Abd Elrahman, M., et al., 2022. Insight into the microstructural and durability characteristics of 3D printed concrete: cast versus printed specimens. *Case Stud. Constr. Mater.* 17, e01320 <https://doi.org/10.1016/j.cscm.2022.e01320>.
- Skibicki, S., Jakubowska, P., Kaszyńska, M., Sibera, D., Cendrowski, K., Hoffmann, M., 2022. Early-age mechanical properties of 3D-printed mortar with spent garnet. *Mater. (Basel)* 15, 1–16.
- Tay, Y.W.D., Qian, Y., Tan, M.J., 2019. Printability region for 3D concrete printing using slump and slump flow test. *Compos Part B Eng* 174, 106968. <https://doi.org/10.1016/j.compositesb.2019.106968>.
- Weng, Y., Li, M., Ruan, S., Wong, T.N., Tan, M.J., Ow Yeong, K.L., et al., 2020. Comparative economic, environmental and productivity assessment of a concrete bathroom unit fabricated through 3D printing and a precast approach. *J. Clean. Prod.* 261, 121245 <https://doi.org/10.1016/j.jclepro.2020.121245>.
- Wolfs, R.J.M., Bos, F.P., Salet, T.A.M., 2018. Cement and Concrete Research Early age mechanical behaviour of 3D printed concrete : numerical modelling and experimental testing. *Cement Concr. Res.* 106, 103–116. <https://doi.org/10.1016/j.cemconres.2018.02.001>.
- Wong, C.L., Mo, K.H., Yap, S.P., Alengaram, U.J., Ling, T.C., 2018. Potential use of brick waste as alternate concrete-making materials: a review. *J. Clean. Prod.* 195, 226–239. <https://doi.org/10.1016/j.jclepro.2018.05.193>.
- Xu, Z., Huang, Z., Liu, C., Deng, X., Hui, D., Deng, S., 2021. Research progress on mechanical properties of geopolymer recycled aggregate concrete. *Rev. Adv. Mater. Sci.* 60, 158–172. <https://doi.org/10.1515/rams-2021-0021>.
- Yang, L., Sepasgozar, S.M.E., Shirovzhan, S., Kashani, A., Edwards, D., 2023. Nozzle criteria for enhancing extrudability, buildability and interlayer bonding in 3D printing concrete. *Autom. Construct.* 146, 104671 <https://doi.org/10.1016/j.autcon.2022.104671>.
- Yu, S., Du, H., Sanjayana, J., 2020. Aggregate-bed 3D concrete printing with cement paste binder. *Cement Concr. Res.* 136, 106169 <https://doi.org/10.1016/j.cemconres.2020.106169>.
- Zhang, Z., Choy, Y., Arulrajah, A., Horpibulsuk, S., 2018. A review of studies on bricks using alternative materials and approaches. *Construct. Build. Mater.* 188, 1101–1118. <https://doi.org/10.1016/j.conbuildmat.2018.08.152>.
- Zhang, B., Zhu, H., Cheng, Y., Huseien, G.F., Shah, K.W., 2022a. Shrinkage mechanisms and shrinkage-mitigating strategies of alkali-activated slag composites: a critical review. *Construct. Build. Mater.* 318, 125993 <https://doi.org/10.1016/j.conbuildmat.2021.125993>.
- Zhang, B., Zhu, H., Feng, P., Zhang, P., 2022b. A review on shrinkage-reducing methods and mechanisms of alkali-activated/geopolymer systems: effects of chemical additives. *J. Build. Eng.* 49, 104056 <https://doi.org/10.1016/j.jobe.2022.104056>.
- Zhao, J., Xie, J., Wu, J., Zhao, C., Zhang, B., 2023. Workability, compressive strength, and microstructures of one-part rubberized geopolymer mortar. *J. Build. Eng.* 68, 106088 <https://doi.org/10.1016/j.jobe.2023.106088>.
- Zhong, H., Zhang, M., 2022. 3D printing geopolymers: a review. *Cem. Concr. Compos.* 128, 104455 <https://doi.org/10.1016/j.cemconcomp.2022.104455>.